Study of the velocity plateau of Dzyaloshinskii domain walls

V. Krizakova,[1,*] J. Peña Garcia,[1] J. Vogel,[1] N. Rougemaille,[1] D. de Souza Chaves,[1] S. Pizzini,[1,†] and A. Thiaville[2,‡]
[1]*Université Grenoble Alpes, CNRS, Institut Néel, F-38000 Grenoble, France*
[2]*Laboratoire de Physique des Solides, Université Paris-Saclay, CNRS UMR 8502, 91405 Orsay, France*

(Received 21 August 2019; published 2 December 2019)

We study field-driven domain wall (DW) velocities in asymmetric multilayer stacks with perpendicular magnetic anisotropy and Dzyaloshinskii-Moriya interaction (DMI), both experimentally and by micromagnetic simulations. Using magneto-optical Kerr microscopy under intense and nanoseconds-long magnetic field pulses, we show that DWs in these films propagate at velocities up to hundreds of meters per second and that, instead of the expected decrease in velocity after the Walker field, a long plateau with constant velocity is observed, before breakdown. Both the maximum speed and the field extent of the velocity plateau strongly depend on the values of the spontaneous magnetization and the DMI strength, as well as on the magnetic anisotropy. Micromagnetic simulations reproduce these features in sufficiently wide strips, even for perfect samples. A physical model explaining the microscopic origin of the velocity plateau is proposed.

DOI: 10.1103/PhysRevB.100.214404

I. INTRODUCTION

The interfacial Dzyaloshinskii-Moriya interaction (DMI) [1,2] in ultrathin magnetic films with perpendicular magnetic anisotropy (PMA) has undergone intensive studies in recent years due to the peculiar field- and current-driven dynamics of noncollinear magnetic textures such as chiral domain walls (DWs) and magnetic skyrmions, which this interaction can stabilize [3–5]. The most important attribute of the DWs gained by the effect of this DMI is their fixed chirality together with the Néel internal structure [6]. The first consequence of this is the shift of the Walker field to larger values, enabling the DWs to reach higher velocity with respect to systems with vanishing DMI [6]. These DWs can also be moved efficiently by an electrical current via the spin-orbit torque associated with the spin Hall effect, reaching higher velocities compared to most systems without DMI [7–10]. Successive DWs move along the same direction as required for racetrack applications [11], making these so-called Dzyaloshinskii DWs attractive for applications in spintronics.

As is well known, one-dimensional (1D) micromagnetics predicts that the velocity of field-driven DWs increases with the applied magnetic field in a steady-state flow regime until it reaches a maximum at a certain threshold, called the Walker field H_W [12–15]. Above it, a sharp decrease in the velocity, called Walker breakdown, occurs, down to the regime of precessional motion where the DW magnetization continuously rotates [13,15], with a constant and lower mobility (the ratio of velocity to field). The breakdown region in which the DW differential mobility is negative is anticipated to be unstable when the sample is two- or three-dimensional [13]. Indeed, in the negative mobility regime, any deformation with respect to a straight DW is amplified. Experimentally, a plateau of velocity beyond the Walker field has often been reported, instead of a negative mobility regime. For bubble garnet films, it was called limiting [16], asymptote [17], or saturation velocity [15,18,19]. A simple two-dimensional (2D) model based on the periodic creation and annihilation of horizontal Bloch lines [20] moving along the sample thickness provided a first analytic expression for this velocity. To describe the experimental results, empirical formulas for this velocity were also proposed [18,19], but without physical justification. More recent experiments have also reported the phenomenon, sometimes more complex than just a plateau. For example, for (Ga,Mn)As films with perpendicular magnetization, a plateau and velocity oscillations were observed [21]. These phenomena could be physically explained by the coupling of the DW global motion to its flexural modes across the thickness, the latter involving both DW position and magnetization [22]. Thus, it appears that the DW dynamics above the Walker field is controlled by processes within the wall, the nature of which depends on the sample characteristics.

In ultrathin films with PMA, the presence of interfacial DMI also strongly modifies the DW dynamics above the Walker field, as shown experimentally [23–25] and reproduced by micromagnetic large-scale simulations [23,24,26]. For sufficiently large DMI, the abrupt DW velocity decrease after the Walker field, expected from 1D theory, is replaced by a velocity plateau before the DW enters the precessional regime for larger fields. This holds provided that the DW is sufficiently long; for narrow strips, up to two breakdowns were observed before reaching the plateau [26]. As ultrathin samples have a thickness well below the micromagnetic exchange length, neither the creation and motion of horizontal Bloch lines seen in bubble garnet films nor the excitation of perpendicular standing spin waves in the DW [22] can be invoked to explain the phenomenon. On the other hand,

*Present address: Laboratory for Magnetism and Interface Physics, Department of Materials, ETH Zurich, 8093 Zurich, Switzerland.
†stefania.pizzini@neel.cnrs.fr
‡andre.thiaville@u-psud.fr

TABLE I. Measured magnetic parameters for the samples whose velocity curves are shown in Fig. 1 and comparison of the measured maximum velocity v_{max} and the end of the velocity plateau B_{break} with simulation results using these parameters, together with $\alpha = 0.15$, with exchange being $A_{ex} = 16$ pJ/m for samples (i) and (ii) and $A_{ex} = 4$ pJ/m for samples (iii) and (iv). The last two columns show the Slonczewski field $\mu_0 H_S$ estimated with Eq. (8) and the Walker field $\mu_0 H_W$ estimated by the 1D model.

Sample	M_s (10^5 A/m)	D (mJ/m^2)	K_{eff} (MJ/m^3)	D/M_s [nJ/(A m)]	v_{max}^{exp} (m/s)	v_{max}^{sim} (m/s)	B_{break}^{exp} (mT)	B_{break}^{sim} (mT)	$\mu_0 H_S$ (mT)	$\mu_0 H_W$ (mT)
(i) Pt/Co(1 nm)/Gd	6.4	1.45	0.26	2.3	640	600	>275	265	325	68
(ii) Pt/Co(1 nm)/GdO$_x$	12.6	1.5	0.44	1.2	300	280	>175	200	225	47
(iii) Pt/GdCo(4 nm)/Ta	2.3	0.2	0.08	0.9	250	230	130	125	140	29
(iv) Pt/GdCo(4.8 nm)/Ta	3.5	0.2	0.06	0.6	160	140	60	35	80	17

micromagnetic simulations highlight the presence of vertical Bloch lines (VBLs) beyond the Walker field. Their creation and annihilation have been claimed to explain the presence of the velocity plateau [23]. In this paper, motivated by experimental observations, we have studied this phenomenon in detail by analyzing the DW structure, the VBLs, and their dynamics for samples presenting different magnetic properties. This allows us to explain the correlation of the velocity plateau with the number of VBLs and, quite surprisingly, to link the field marking the end of the plateau to the DMI field stabilizing the DWs in the Néel structure.

II. EXPERIMENTS

Domain wall velocity versus easy-axis magnetic fields B_z were measured for four samples characterized by very different values of spontaneous magnetization M_s and DMI strength D, which, as we will show, are at the origin of the different behaviors of the domain wall dynamics: (i) Pt/Co(1 nm)/Gd/Al, (ii) Pt/Co(1 nm)/GdO$_x$/Al, (iii) Pt/GdCo(4 nm)/Ta, and (iv) Pt/GdCo(4.8 nm)/Ta (layers are listed from bottom to top). The first two multilayer stacks were studied in detail in Ref. [24]. The samples were prepared by magnetron sputtering on Si/SiO$_2$ substrates [24]. The Gd$_x$Co$_{1-x}$ layers with composition gradient $x \sim 0.21$–0.23 were prepared by cosputtering of Gd and Co targets [27]. Because of the vicinity of the composition compensation at room temperature (RT), the magnetization is strongly reduced in these two samples. Moreover, since the compensation temperature in these alloys is very sensitive to the composition, their RT magnetizations differ. The material parameters of the four samples are summarized in Table I. Magnetization M_s and effective anisotropy K_{eff} were measured by magnetometry, whereas the DMI parameter D was estimated from the in-plane field dependence of the DW velocity in the flow regime. The details of the Kerr microscopy experiments allowing the measurement of DW velocities as a function of B_z and of the DMI strength are also described in Ref. [24]. In that work, we showed that the field-driven domain wall velocity after the Walker field is tuned by the ratio D/M_s between the DMI strength [$D \sim 1.5$ mJ/m^2 for samples (i) and (ii)] and the spontaneous magnetization M_s. While, for Pt/Co/GdO$_x$, M_s at RT is close to the bulk value (1.26 MA/m), a strong reduction of M_s is observed in Pt/Co/Gd, where an interfacial ferrimagnetic alloy forms at the top Co interface. The saturation DW velocity at high field, of the order of 300 m/s in Pt/Co/GdO$_x$, increases up to 600 m/s in Pt/Co/Gd due to the lower magnetization. In both samples, the velocity plateau extends up to the largest fields for which the speeds could be measured (Fig. 1, left panel). The situation is different for the Pt/GdCo/Ta trilayers where the magnetization M_s as well as the DMI are reduced (see Table I). The maximum velocities are smaller than in the previous samples, and moreover, while in sample (iii) a drop in the velocity is observed around 100 mT, in sample (iv) the velocity drops soon after the Walker field, at around 60 mT. The saturation velocity and the velocity breakdown field for the four samples are reported in Table I. In the following, we show that 2D numerical simulations reproduce quantitatively the different behaviors of the DW velocity in the four samples and propose a physical understanding of all the results.

III. CALCULATION METHODS

Micromagnetic simulations were realized using the MUMAX3 software [28], which solves the Landau-Lifshitz-Gilbert equation in finite-difference discretization. The initial material parameters $M_s = 1.26$ MA/m, $D = 1.5$ mJ/m^2, $K_{eff} = 0.44$ mJ/m^3, $A_{ex} = 16$ pJ/m, and magnetic damping constant $\alpha = 0.15$ were selected to imitate the magnetic properties of sample (ii). Although disorder is absent in the simulations presented here, we have verified that it does not affect the main results of this work. Subsequently, M_s, K_{eff}, and D were varied in order to cover the range of values obtained experimentally for the other trilayers. In the simulations, a Néel wall introduced into the strip-shaped sample is displaced by the action of a magnetic field normal to the plane, as sketched in Fig. 2, within a $(1 \times 1)\,\mu$m^2 moving-frame window (to keep the domain wall in its center). The lateral mesh is chosen to

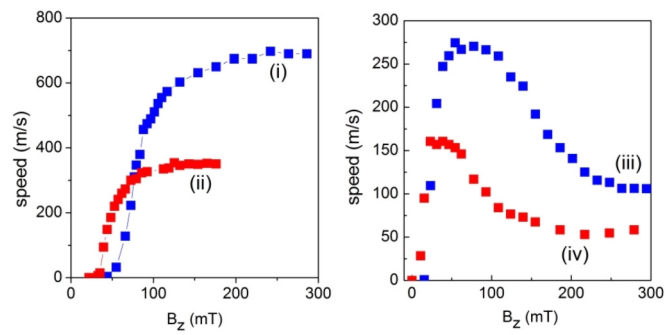

FIG. 1. Domain wall velocity versus easy-axis field B_z measured for (i) Pt/Co(1 nm)/Gd, (ii) Pt/Co(1 nm)/GdO$_x$, (iii) Pt/GdCo(4 nm)/Ta, and (iv) Pt/GdCo(4.8 nm)/Ta.

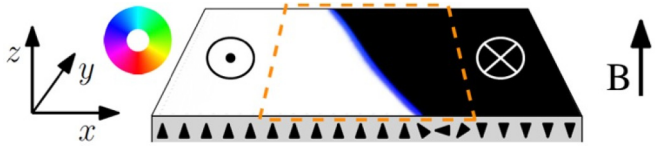

FIG. 2. Scheme of simulation geometry with the depicted micromagnetic spin configuration. White (black) corresponds to magnetization upward (downward), and the color wheel shows the orientation of the in-plane magnetization component. The framed region depicts the moving calculation window.

be $\approx(2 \times 2)\,\mathrm{nm}^2$, which is sufficiently accurate with respect to the DW width parameter $\Delta = \sqrt{A_{ex}/K_{eff}}$, equal to 5–10 nm in the cases examined here.

The dynamics of a DW in perpendicularly magnetized nanostrips of different widths was first studied to explore the transition between the 1D and 2D behaviors. For widths larger than 500 nm the DW dynamics displayed the characteristics observed experimentally, i.e., large DW speeds with a plateau of maximum velocity. Consequently, the strip width of 1 μm was selected for all computations.

The micromagnetic configurations were analyzed by first finding the precise DW path. Having located the DW at the bottom edge of the calculation box, the DW was followed as it crossed successive horizontal or vertical mesh lines between the mesh points. To analyze the DW magnetic structure, the tangential and normal components of the DW (in-plane) magnetization were then computed. In addition, the local in-plane angle φ of the DW magnetization, counted from the DW tangent and, for continuity, not restricted to the $[0, 2\pi]$ interval, was evaluated starting from the strip y bottom (see axis definitions in Fig. 2). Thus, $\varphi = 0$ is a left-handed Bloch wall, $\varphi = \pi/2$ is a left-handed Néel wall, etc. VBLs were identified by processing the profile of φ versus curvilinear abscissa s along the DW. The statistics shown below (number and density of 2π VBLs, DW length, etc.) were obtained on 500 snapshots from 10 DW configurations, obtained by running a single calculation for 500 ns and collecting 50 snapshots at a 1 – ps interval, with a 50-ns interval between two configurations. Indeed, as the DW configuration does not change enough on the nanosecond timescale, measurements on a single DW configuration show excessive scatter.

IV. SIMULATION RESULTS AND ANALYSIS

Figures 3(a) and 3(b) show the simulated velocity vs field curves for different D or M_s values while keeping the other parameters constant. The DW velocity v_W at the Walker field H_W is seen to increase linearly with the DMI strength D and to decrease as the magnetization M_s increases. These results agree with the previously derived analytic formula (the last equality holds when the DMI field is much larger than the internal demagnetizing field of the Néel wall):

$$v_W = \gamma_0 \frac{\Delta}{\alpha} H_W \approx \frac{\pi}{2} \gamma_0 \Delta H_{DMI} = \frac{\pi}{2} \gamma \frac{D}{M_s}, \qquad (1)$$

where γ is the gyromagnetic ratio, $\gamma_0 = \mu_0 \gamma$, and $H_{DMI} = D/(\mu_0 M_S \Delta)$ is the DMI field that stabilizes the DW in the

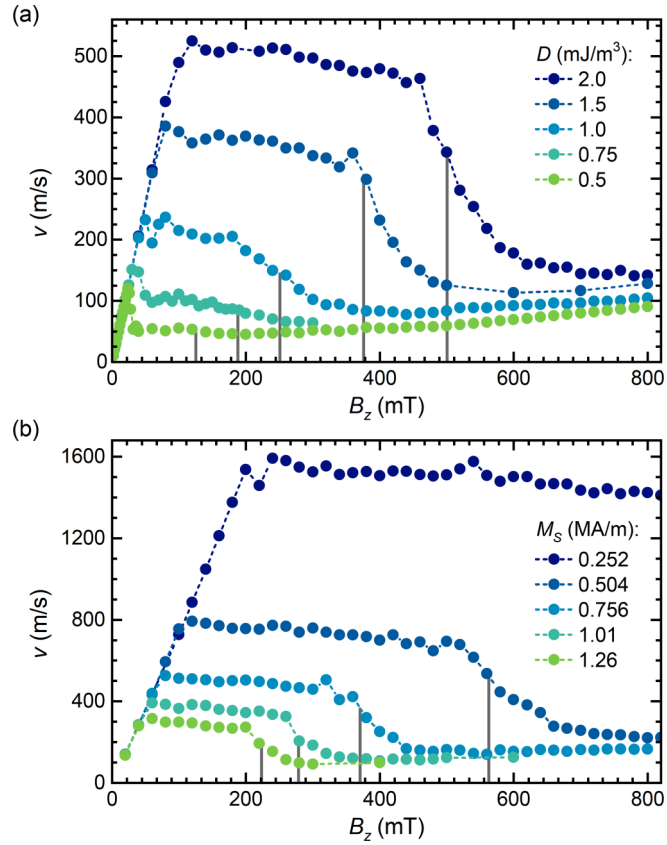

FIG. 3. Simulated field-driven DW velocity for (a) $M_s = 1.01\,\mathrm{MA/m}$ and $K_u = 1.44\,\mathrm{mJ/m^3}$ so that $K_{eff} = 0.80\,\mathrm{mJ/m^3}$ and different values of DMI strength and (b) fixed $D = 1.5\,\mathrm{mJ/m^2}$, $K_{eff} = 0.44\,\mathrm{mJ/m^3}$ and varying spontaneous magnetization. The different lengths of the velocity plateau for $D = 1.5\,\mathrm{mJ/m^2}$ and $M_s = 1.01\,\mathrm{MA/m}$ in (a) and (b) result from the different K_{eff} values (see discussion later in the text). The vertical segments mark the computed Slonczewski fields according to Eq. (8).

Néel configuration. They also agree with the results of domain wall velocity measurements [24].

The simulations also show that, in agreement with experiments, the velocity is nearly constant for a certain field range above the Walker field and that the length (in field scale) of this velocity plateau is also dependent on D and M_s. In the case of strong DMI [e.g., $D = 1.5\,\mathrm{mJ/m^2}$ as in Fig. 3(b)], one sees that the plateau length decreases as M_s increases. On the other hand, Fig. 3(a) shows that for a constant $M_s = 1.01\,\mathrm{MA/m}$, the length of the plateau decreases as D decreases, with the plateau even disappearing for low DMI values (e.g., $D \leqslant 0.5\,\mathrm{mJ/m^2}$). Therefore, a first parameter determining both the saturation speed and the field extension of the velocity plateau appears to be the ratio between the DMI strength and the spontaneous magnetization. Experimentally, both the saturation velocity and the plateau extension indeed decrease as this ratio decreases (see Fig. 1 and Table I). Figure 3, in addition, shows that the plateau length is also related to the domain wall width $\pi\sqrt{A_{ex}/K_{eff}}$. To understand the microscopic mechanism leading to the velocity plateau and its breakdown, the DWs need to be examined more closely by following the evolution of their magnetic structure and shape in different applied fields and as a function of time.

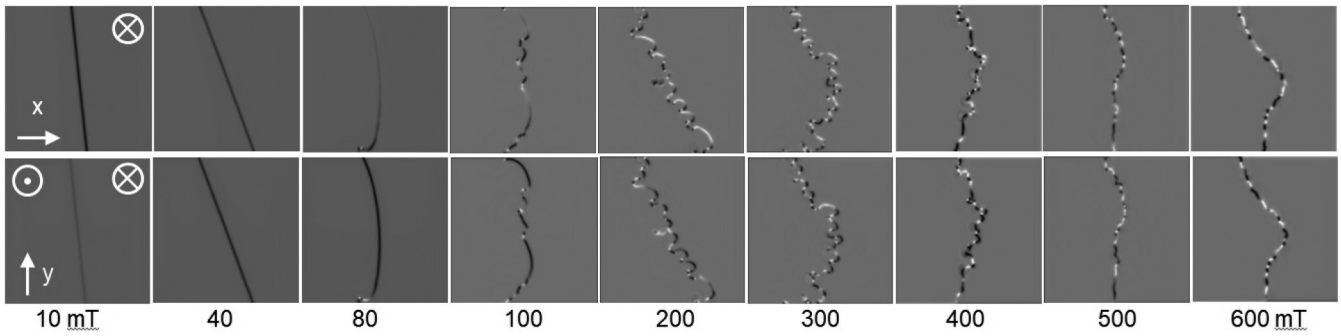

FIG. 4. Sequence of images of the normalized magnetization components m_x and m_y (along and perpendicular to the strip direction) in $(1 \times 1)\,\mu\text{m}^2$ moving windows for different driving fields. The orientation of the magnetization vector in both domains is indicated in the first frame. The displayed magnetization component is indicated by an arrow (white = parallel, black = antiparallel to the arrow). Each frame is captured more than 50 ns after field application, when the DW has reached a stable configuration. Simulation parameters are $M_s = 0.756\,\text{MA/m}$, $D = 1.5\,\text{mJ/m}^2$, $K_u = 0.80\,\text{mJ/m}^3$, $A_{ex} = 16\,\text{pJ/m}$.

Figure 4 shows, for increasing magnitude of the applied field B_z, images of the magnetization components in the x and y directions in the case of a strip with $M_s = 0.756$ MA/m, $K_u = 0.80$ mJ/m^3, so that $K_{\text{eff}} = 0.44$ mJ/m^3 and $D = 1.5$ mJ/m^2. Several trends can be identified, corresponding to the different dynamical regimes shown by the corresponding velocity curve [Fig. 3(b), middle curve]. For low fields and up to the Walker field ($\simeq$77 mT), the domain wall is straight and tilted with respect to the stripe direction, with the tilt angle initially increasing with field [29]. Also, the DW magnetization rotates from the (left-handed) Néel wall orientation and becomes close to a (right-handed) Bloch wall orientation as the Walker field is approached, as expected [6] (see image at 80 mT). Above the Walker field, a sudden transition to a turbulent regime occurs. The domain wall length increases with respect to the low-field case and acquires a meander shape, with an increasing number of curls, up to the end of the velocity plateau at around 350 mT. This behavior has already been observed in Refs. [23,24,26]. After reaching the maximum length, at the end of the plateau, the DW rapidly shortens but remains meandering. With increasing field, it slowly straightens, and its magnetization reaches a coherent precessional regime at around 0.5 T. In parallel, the in-plane magnetization images reveal a multiplication of sign changes. When the DW is straight, this directly means that the DW magnetization spatially rotates between the Bloch and Néel orientations. On the other hand, when the DW is strongly meandering, the local magnetization orientation, i.e., its angle φ relative to the DW tangent, should be scrutinized in order to determine if the DW is Néel or Bloch and if a VBL is present. This analysis is detailed in the Appendix.

In order to have a global view of the DW magnetic structure, the histograms of local DW magnetization angles are shown in Fig. 5 separately for the plateau region (80–350 mT) and beyond the plateau. Just above the Walker field, the distribution has a strong peak close to $\varphi = \pi$, the right-handed Bloch wall derived from the left-handed Néel wall by $\pi/2$ precession. It is therefore justified to describe the DW as a chiral Bloch wall, as proposed previously [23,26]. As the field increases, the intensity of this peak diminishes, whereas the background intensity increases, with a preference for the energetically favored left-handed Néel wall. On the other hand, at large fields the histogram is increasingly flat.

From the profiles of local DW magnetization angle $\varphi(s)$, the processes involving the vertical Bloch lines were investigated. As known from bubble physics [15], in achiral Bloch walls four types of VBLs exist, degenerate in energy and grouped into two senses of winding [30], corresponding to $\pm\pi$ rotations of φ, the stable orientations for the DW moment being $\varphi = 0, \pi$. In the presence of interfacial DMI, it was proposed [23] that these four VBL types separate into those that are favored, with a core magnetization parallel to the DMI effective field, and those that are unfavored. This scheme implicitly rests on the concept of an underlying achiral Bloch wall. This is, however, not the static state, which due to an interfacial DMI is a chiral Néel wall. Dynamically, just before the Walker breakdown, this DW does transform into a Bloch wall, but it is chiral as it derives from the rest structure by $\pi/2$ precession around the applied field [6,23]. Hence, when DMI dominates over DW internal magnetostatics, only a 2π VBL is a relevant object. In static conditions it separates two chiral Néel walls with $\pm 2\pi$ difference in φ [Figs. 6(a) and 6(b)], while just below the Walker threshold it separates two chiral Bloch walls [Figs. 6(c) and 6(d)]; this conclusion was also reached by Ref. [31]. Note that, in the latter situation, if one fictively decomposes the 2π VBL into two 1π VBLs, a slower magnetization rotation (larger width) is indeed observed for the VBL favored by DMI compared to the unfavored one (Fig. 9), in accordance with the arguments of Ref. [23]. Therefore, we used as the operational 2π VBL definition the fact that φ changes by 2π, the sense of variation giving the VBL winding. This procedure, starting from the y bottom of the DW where the DW magnetization also varies with time, cannot be used to locate precisely the VBLs but, at least, is accurate for determining the number of VBLs and their winding.

Figure 7 summarizes the results of the detailed analysis of the shape and magnetic profile of the moving DWs. It appears that the variation of the DW velocity is correlated to the DW length, to the total number of 2π VBLs, and, but less clearly, to the density ρ of 2π VBLs. Below the Walker field, the domain wall is straight and without VBLs. Above the Walker field but within the velocity plateau, the domain wall

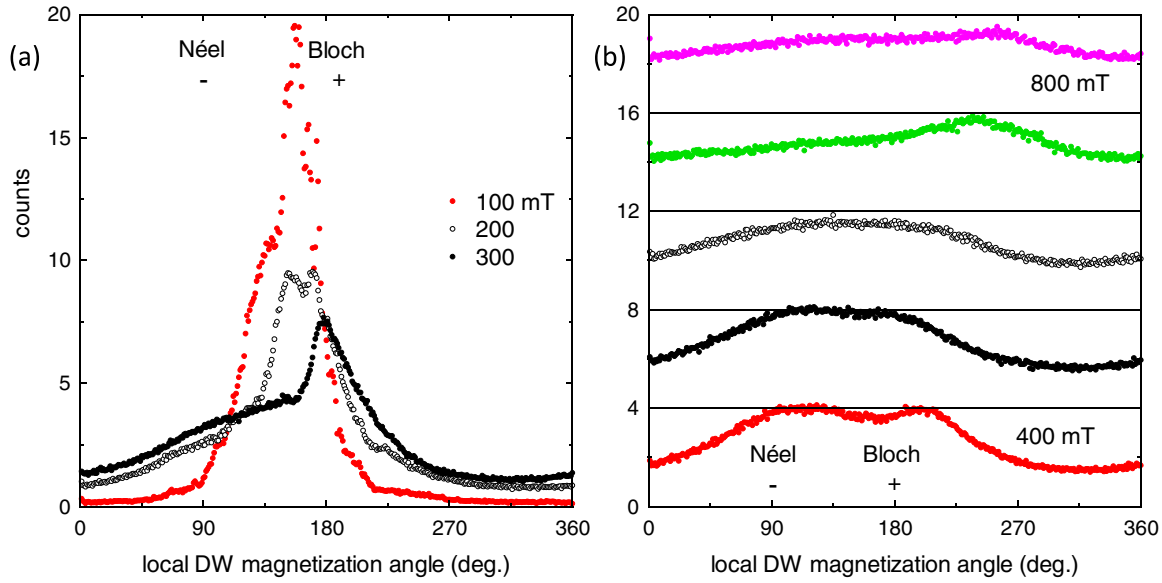

FIG. 5. Distribution of the local DW magnetization angle φ for several applied fields, (a) within the velocity plateau and (b) above it. Parameters are $M_s = 0.756\,\mathrm{MA/m}$, $K_{\mathrm{eff}} = 0.44\,\mathrm{mJ/m^3}$, and $D = 1.5\,\mathrm{mJ/m^2}$. For each field, the 10×50 acquired DW snapshots were processed, realizing a space and time average of the DW magnetization angle. The histogram binning is 1°, and the vertical scale is for 1000 counts in total. In (b), curves are vertically offset (by 4 units) for clarity.

length and the number of 2π VBLs increase. Both decrease abruptly, like the velocity, when the plateau ends. On the other hand, the 2π VBL density increases inside the plateau but peaks after it has terminated and then slowly decreases. After the plateau, the velocity progressively merges into the precessional velocity regime with low mobility, as predicted by the one-dimensional (q, Φ) model.

In order to see if the maximum 2π VBL density accommodated by the DW is a relevant parameter, we compare it to the value deduced from the estimated 2π VBL size. An approximate calculation of its extent can be made under the assumptions that the domain wall remains straight and that the DMI dominates the domain wall internal demagnetizing effect. The resulting energy takes the same form as that of the classical Bloch wall profile, only with an angle scaled by a factor of 2. We thus find that the 2π VBL width S (using the conventional Lilley definition in terms of the tangent to the angle profile at the central point [32]) reads

$$S = 2\pi\sqrt{A_{\mathrm{ex}}\Delta/(\pi D)}. \tag{2}$$

Compared to these analytical models, full numerical calculations show that the domain wall bends at the 2π VBL for magnetostatic reasons, a feature noticed long ago [33,34] and analytically obtained recently [31]. One gets that the maximum 2π VBL density is about a quarter of the inverse size. This means that the end of the velocity plateau is not given by the uniform rotation model [15] in which VBLs are densely packed.

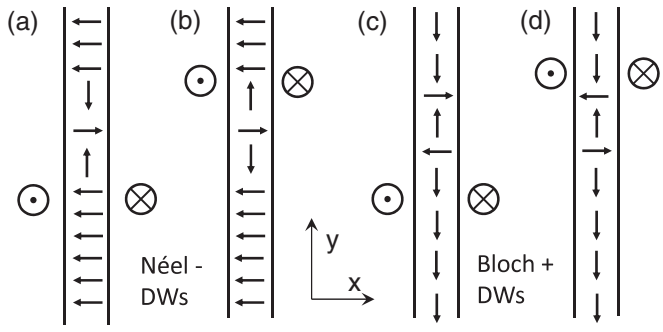

FIG. 6. Scheme of 2π VBLs in Dzyaloshinskii domain walls (a) and (b) in statics and (c) and (d) around the Walker field under positive z field drive. The winding of the 2π VBL is opposite between (a) and (b), and between (c) and (d).

V. DISCUSSION

A framework to analyze the DW dynamics above the Walker field is provided by the Slonczewski equations [13,35]. For the present situation, their variables are the local DW x position $q(y,t)$, a function of the y position across the strip and time t, and the angle of DW magnetization $\Phi(y,t)$ in the absolute frame. For large corrugations of the DW, one should rather use $q(s,t)$ and $\Phi(s,t)$, where s is the curvilinear abscissa and the DW local displacement q is measured along the normal to the DW [15,36], but we ignore this subtlety in this qualitative analysis. When the DW is not straight, the equations indicate that the DW surface energy induces an additional field H_q parallel to the applied field, proportional to the DW curvature (in magnitude and sign)

$$H_q = \frac{\sigma}{2\mu_0 M_S}\frac{\partial^2 q}{\partial y^2}, \tag{3}$$

where $\sigma = 4\sqrt{A_{\mathrm{ex}}K_{\mathrm{eff}}} - \pi D$ is the DW surface energy density. Note that this field also appears in the creep theory of magnetic domain walls [37]. As shown in Fig. 8, H_q decreases the drive field at the places that are ahead of the average DW position and increases it at the places that lag behind. The typical value of this field is not at all negligible: for the

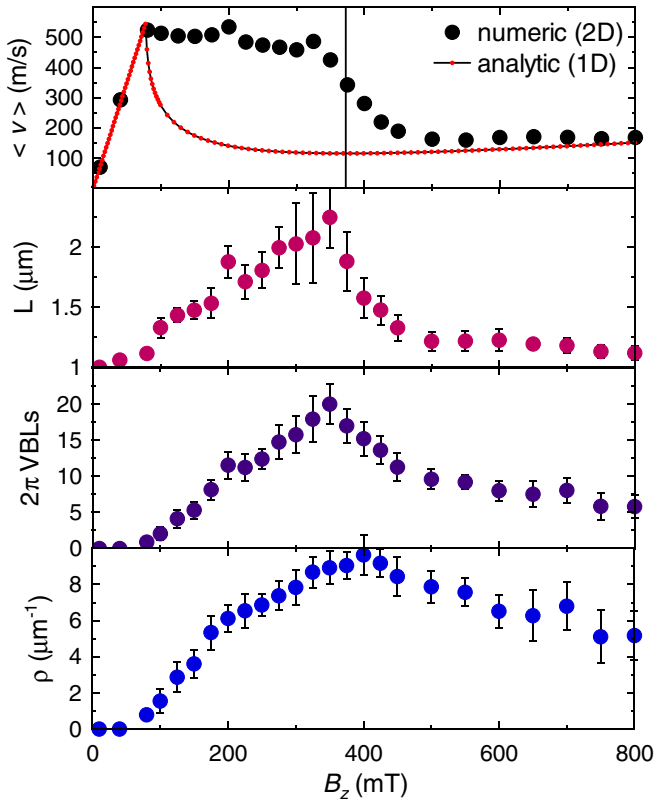

FIG. 7. Field dependency of DW parameters: velocity, length, number of 2π VBLs inside the DW, and 2π VBL density ρ in a 1-μm-wide strip, with $M_s = 0.756\,\mathrm{MA/m}$, $K_{\mathrm{eff}} = 0.44\,\mathrm{mJ/m^3}$, and $D = 1.5\,\mathrm{mJ/m^2}$. The red velocity curve expresses the analytical 1D model (in the limit where the DMI field is much larger than the demagnetizing field of the Néel wall) for the corresponding micromagnetic parameters, with the computed Slonczewski field according to Eq. (8) indicated by a vertical line.

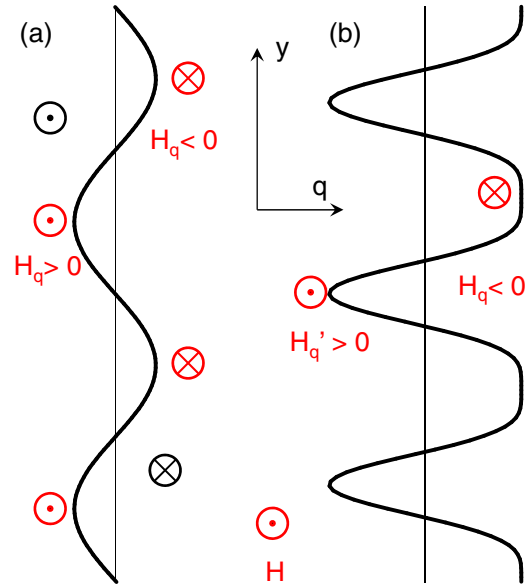

FIG. 8. Sketch of corrugated domain walls. (a) For a sinusoidal profile, the curvature-induced fields [Eq. (3)] are equal and opposite at the two extremities of the DW, and a larger total field is applied to the part of the DW lagging behind. (b) For a corrugated profile with smaller zones lagging behind, these experience a yet larger field. This last configuration resembles the images of Fig. 4. Magnetizations are drawn in black, and fields are in red.

parameters of Fig. 7 one has $\sigma = 5.9\,\mathrm{mJ/m^2}$, so that a sine modulation with an amplitude of ± 50 nm and wavelength of 200 nm produces $\mu_0 H_q = 192\,\mathrm{mT}$.

Based on these ideas, a heuristic "corrugated wall" regime was proposed by Slonczewski [13] for the DW dynamics above the Walker field in the negative mobility region, in which $H + H_q \leqslant H_{\mathrm{W}}$ for the DW parts which are ahead, whereas in the lagging parts $H + H_q \gg H_{\mathrm{W}}$. The increased field in the lagging parts causes a faster precession of DW magnetization, hence driving the nucleation of VBLs, corresponding to the observations. As a corrugated DW is longer, the increase of both DW length and VBL number seen in Fig. 7 is consistent with this mechanism. The corrugated wall picture also corresponds well to the DW images shown in Fig. 4 for $\mu_0 H_z = 100$ and 200 mT. In Ref. [13] Slonczewski then looked for a steady-state DW corrugation and associated velocity. The numerical simulations show, however, that the situation is more complex, so Slonczewski's model cannot be directly applied. Nevertheless, despite the complexity of the DW shape and magnetization profile, some integral relations hold that help us understand this regime.

The first is the "momentum conservation," i.e., the spatial and temporal average of the first Slonczewski equation, given by

$$\left\langle\left\langle \frac{\partial \Phi}{\partial t} \right\rangle\right\rangle + \frac{\alpha}{\Delta}\left\langle\left\langle \frac{\partial q}{\partial t} \right\rangle\right\rangle = \gamma_0 H, \tag{4}$$

where the double brackets indicate the two averages. This is the version of the DW dynamics model under the assumption of a constant DW width parameter Δ, but it has been shown that this equation can be generalized to arbitrary spin textures [38], upon definition of a generalized Φ angle and DW position. In the present case, if $H > H_{\mathrm{W}}$ and the DW moves at an average velocity $v \approx v_{\mathrm{W}}$, one gets $\langle\langle \partial\Phi/\partial t \rangle\rangle \approx \gamma_0 (H - H_{\mathrm{W}})$. This means that DW magnetization precession is required for fast DW motion above the Walker field, contrary to a naive expectation that DW magnetization precession equals velocity breakdown. In the corrugated DW model, this precession is localized in the lagging DW parts, and the momentum conservation is satisfied if the length fraction f of these parts and the curvature-induced field H_q satisfy $f\sqrt{(H + H_q)^2 - H_{\mathrm{W}}^2} \approx H - H_{\mathrm{W}}$, a relation that can be approximated to $(H + H_q) f \approx H - H_{\mathrm{W}}$ for large H. Inspection of Fig. 4 for $\mu_0 H_z = 100$ and 200 mT reveals that f indeed increases with H.

The second relation is simply the energy balance [13]: by the DW motion the total energy of the sample decreases at a rate $-2\mu_0 M_{\mathrm{S}} H v$ per unit cross section of the strip. In the micromagnetic dynamics equation, energy decreases only by the damping term, with a volumetric dissipative power given by $-\alpha(\mu_0 M_{\mathrm{S}}/\gamma_0)(\partial \vec{m}/\partial t)^2$. The obvious source of magnetization time variation is the DW, and the two DW mobility regimes can be obtained by evaluating this energy dissipation. But in addition, the DW can emit spin waves that

disappear inside the domains, dissipating energy as well. As detailed in the Appendix, spin waves are emitted when a 2π VBL disappears, releasing its energy. At rest, still neglecting deformation of the DW profile in its vicinity, the energy of a 2π VBL is analytically evaluated as

$$\lambda = 16\sqrt{A_{\rm ex}\Delta\pi D} \tag{5}$$

per unit length (the thickness of the film). The number of 2π VBLs disappearing per unit time can be estimated from the time evolution of the profiles of the local angle φ (see the Appendix). We find that the energy dissipated by this process amounts to about one third of the required additional energy dissipation compared to that of a 1D DW moving at the Walker velocity, namely, $-2\mu_0 M_{\rm S}(H - H_{\rm W})v_{\rm W}$. In fact, the energy dissipated by the destruction of the 2π VBLs is at least twice as large as this estimation, as the comparison of numerical and analytical $\varphi(s)$ profiles shows that the dynamical 2π VBLs are compressed by a factor larger than 4, leading to a larger dissipation upon annihilation. This shows that the VBL-based energy loss mechanism is quantitatively dominant in the velocity plateau at the Walker velocity.

We finally discuss the end of this plateau. A first remark is that the field where the plateau ends is close to the field where the 1D model predicts the velocity to be the minimum (see Fig. 7). This field was considered apparently only by Slonczewski [13,20] and may therefore be called the Slonczewski field $H_{\rm S}$. In the 1D model with purely second-degree DW effective anisotropy K_{DW} leading to a DW internal anisotropy field $H_{K_{DW}} = 2K_{DW}/(\mu_0 M_{\rm S})$, which is analytically solvable, one has $H_{\rm W} = \alpha H_{K_{DW}}/2$ and $v_{\rm W} = \gamma_0 \Delta H_{K_{DW}}/2$ for the Walker threshold, whereas for the Slonczewski minimum the quantities are [13]

$$H_{\rm S} = H_{K_{DW}} \frac{1+\alpha^2}{2\sqrt{2+\alpha^2}} \approx H_{K_{DW}}/(2\sqrt{2}), \tag{6}$$

$$v_{\rm S} = \gamma_0 \Delta H_{K_{DW}} \frac{\alpha\sqrt{2+\alpha^2}}{2(1+\alpha^2)} \approx \gamma_0 \Delta H_{K_{DW}} \frac{\alpha}{2}, \tag{7}$$

with the approximations holding for $\alpha \ll 1$.

In our case, when the DMI-induced field satisfies $H_D \gg H_{K_{DW}}$, this 1D model applies (just consider $\Phi/2$ to be the angular variable), and one has [6] $H_{\rm W} \approx \alpha H_D$, so that

$$H_{\rm S} = \frac{1+\alpha^2}{\sqrt{2+\alpha^2}} H_D = \frac{\pi(1+\alpha^2)}{2\sqrt{2+\alpha^2}} \frac{D}{\mu_0 M_{\rm S}\Delta}, \tag{8}$$

where the numerical factor is 1.11 in the small-α limit, so that $H_{\rm S} \approx H_{\rm DMI}$ [remember that $H_D = (\pi/2)H_{\rm DMI}$].

One sees that the dependence of $H_{\rm S}$ on the micromagnetic parameters D and M_s is exactly that found in the experiments and the simulations and, moreover, that the agreement with both is quantitatively very good. It also confirms that the length of the velocity plateau is related to the DW width, as already found in the simulations. This can be taken as a hint that the corrugated wall model is relevant for the dynamics above the Walker field, with the plateau lasting at most up to the field where the driving force for the corrugation instability disappears.

Regarding the value of the plateau velocity, we have only qualitative arguments. Within the corrugated wall model, the corrugation instability cannot grow beyond reaching $H + H_q = H_{\rm W}$ in the leading edge parts, so that one has $v \leqslant v_{\rm W}$. We have also seen that the momentum and energy conservation relations can be satisfied in this model by localized precession in the lagging behind parts and 2π VBL destruction, respectively, when the DW moves close to the Walker velocity. This shows that $v \approx v_{\rm W}$ is an admissible solution in the negative mobility regime. The specificity of large DMI values is that, on top of a large Walker field and Walker velocity, the DMI forces the formation of 2π VBLs, which can store a large amount of energy which can be released upon annihilation. A large DMI also leads to a large Slonczewski field, the apparent end of the velocity plateau, which therefore becomes easier to observe.

VI. CONCLUSION

We have experimentally shown that, for chiral Néel walls stabilized by the interfacial Dzyaloshinskii-Moriya interaction (Dzyaloshinskii domain walls), the maximum velocity and the end of the high-velocity plateau are controlled mainly by the ratio $D/M_{\rm s}$ of DMI to spontaneous magnetization. This observation has been confirmed by systematic 2D micromagnetic simulations. These additionally revealed that the domain wall width also impacts the end of the high-velocity plateau and that the moving domain wall is strongly corrugated in the plateau region. A detailed analysis of the domain wall in-plane magnetization variation along its length has shown the key role of 2π vertical Bloch lines, textures that are topologically stable and therefore disappear through a Bloch point, dissipating a large energy through the emission of spin waves. We propose that this plateau corresponds to the negative mobility regime of the one-dimensional domain wall dynamics, as qualitatively described by the corrugated domain wall model of Slonczewski. As a result, the end of the high-velocity plateau is simply proportional to the effective DMI field, with a numerical factor independent of damping in the low-damping limit.

ACKNOWLEDGMENTS

This work was realized with the support of the Erasmus+ program of the European Union. S.P., J.V., and A.T. acknowledge the support of the Agence Nationale de la Recherche, projects ANR-14-CE26-0012 (ULTRASKY) and ANR-17-CE24-0025 (TOPSKY). D.d.S.C. was supported by a CNPq Scholarship (Brazil). J.P.G. acknowledges the European Union's Horizon 2020 research and innovation program under Marie Sklodowska-Curie Grant Agreement No. 754303 and the support from the Laboratoire d'excellence LANEF in Grenoble (ANR-10-LABX-0051). We thank B. Fernandez, Ph. David, and E. Mossang for technical help. A.T. thanks J. Miltat, S. Rohart, and J. Sampaio for inspiring discussions.

APPENDIX: ANALYSIS OF THE MAGNETIC STRUCTURE OF THE DOMAIN WALLS

The profiles of the local magnetization angle φ for the DWs presented in Fig. 4 at zero relative time, together with their time evolution, are plotted in Fig. 9 for selected field values.

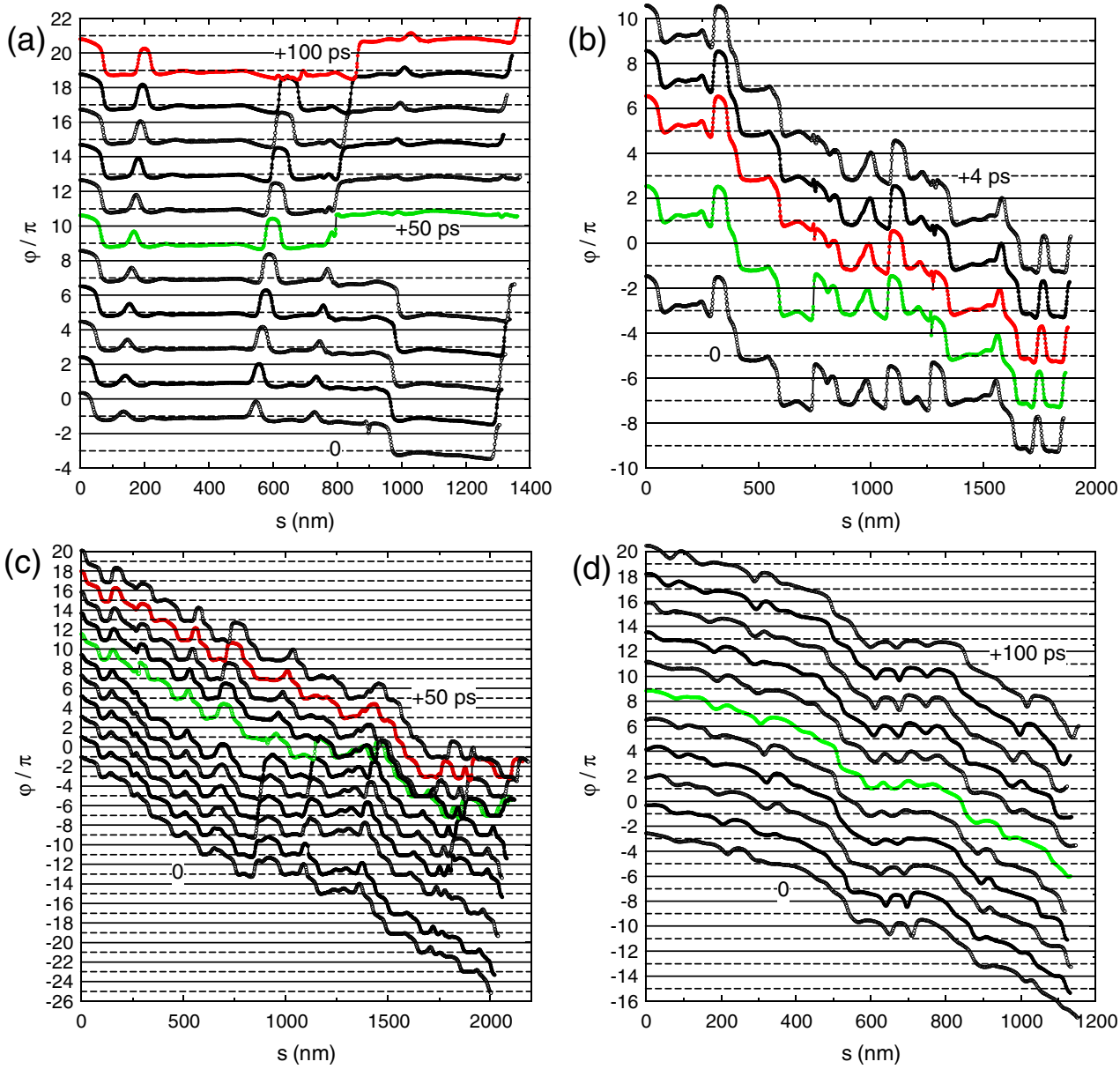

FIG. 9. Time evolution of the profiles of the local magnetization angle φ for the DWs presented in Fig. 4. The applied fields are (a) $B_z =$ 100, (b) 200, (c) 300, and (d) 500 mT. The relative times (ps) are indicated, and the profiles are successively offset by (multiples of) 2π for clarity. The dashed horizontal lines indicate the dynamically favored chiral Bloch wall orientations. Profiles are colored to highlight changes or help differentiate them. The origin of the curvilinear abscissa (s) is at the bottom of the images.

The local DW magnetization angles are counted relative to the DW tangent direction (globally along $+y$ as the DW is followed from bottom to top) in the trigonometric sense so that $\varphi = \pi/2$ is the left-handed Néel wall and $\varphi = \pi$ is the right-handed Bloch wall. One notices that for all profiles φ globally decreases with increasing curvilinear abscissa s. Taking into account that, in the presence of DMI, the DW magnetization precession starts at a given edge of the strip [26] (here the bottom edge; see the image at 80 mT in Fig. 4) and that the applied field is positive, this can be rationalized.

In Fig. 9(a), corresponding to $B_z = 100$ mT, the progressive precession of DW magnetization is shown: a precession from $\simeq 0.3\pi$ to $\simeq 1.5\pi$ takes place at $s \approx 150$ nm, and a precession from $\simeq 1\pi$ to 2π is observed at $s \approx 600$ nm. In the latter case, the two 2π VBLs that have formed disappear (at a 1-ps interval) between the last two profiles. The last curve shows a signature of the spin-wave wake emitted after the 2π VBLs destruction. This corresponds to the main mode observed. More rarely, especially just above the Walker field, the conversion of one VBL of the pair into another one, with thus opposite winding and core magnetization, is seen. These two lines, having opposite winding senses, merge back into a 2π VBL, which eventually disappears, as shown above. Such a process is observed at $s \approx 800$ nm.

Figure 9(b), corresponding to $B_z = 200$ mT, shows that the 2π VBL destruction is extremely fast. In fact, the process is instantaneous as the annihilation of the topologically stable 2π VBL involves a Bloch point crossing the sample

thickness [15,39]. As the sample is described by one layer of cells, this Bloch point is numerically virtual (there is no interval between layers of mesh points where it could sit). One 2π VBL disappears between times 30 and 31 ps, at $s \approx 1250$ nm, and another one disappears between times 31 and 32 ps, at $s \approx 750$ nm. The propagation of the spin-wave wake is also observed on the $\varphi(s)$ profiles.

For a larger field $B_z = 300$ mT [Fig. 9(c)], still within the velocity plateau, the same processes are seen. The VBLs are, however, less visible as the overall slope of $\varphi(s)$ has increased. Finally, for $B_z = 500$ mT [Fig. 9(d)], beyond the velocity plateau, the dominant time evolution is the global precession of the DW magnetization, but 2π VBL destructions occur from time to time. We thus have a global picture of the time evolution of the angles φ: they increase with time in a nonuniform way by the formation of unwinding VBL pairs, with the continued precession transforming these pairs into $2 \times 2\pi$ "pairs of pairs." Each 2π VBL can disappear through the passage of a Bloch point, releasing its energy by spin-wave emission.

[1] I. E. Dzyaloshinskii, Sov. Phys. JETP **5**, 1259 (1957).
[2] T. Moriya, Phys. Rev. **120**, 91 (1960).
[3] S. Heinze, K. von Bergmann, M. Menzel, J. Brede, A. Kubetzka, R. Wiesendanger, G. Bihlmayer, and S. Blügel, Nat. Phys. **7**, 713 (2011).
[4] G. Chen, T. Ma, A. T. N'Diaye, H. Kwon, C. Won, Y. Wu, and A. K. Schmid, Nat. Commun. **4**, 2671 (2013).
[5] A. Fert, V. Cros, and J. Sampaio, Nat. Nanotechnol. **8**, 152 (2013).
[6] A. Thiaville, S. Rohart, É. Jué, V. Cros, and A. Fert, Europhys. Lett. **100**, 57002 (2012).
[7] T. A. Moore, I. M. Miron, G. Gaudin, G. Serret, S. Auffret, B. Rodmacq, A. Schuhl, S. Pizzini, J. Vogel, and M. Bonfim, Appl. Phys. Lett. **93**, 262504 (2008).
[8] I. M. Miron, T. Moore, H. Szambolics, L. D. Buda-Prejbeanu, S. Auffret, S. Rodmacq, B. Pizzini, J. Vogel, M. Bonfim, A. Schuhl, and G. Gaudin, Nat. Mater. **10**, 419 (2011).
[9] K.-S. Ryu, L. Thomas, S.-H. Yang, and S. Parkin, Nat. Nanotechnol. **8**, 527 (2013).
[10] S. Emori, U. Bauer, S.-M. Ahn, E. Martinez, and G. Beach, Nat. Mater. **12**, 611 (2013).
[11] S. S. P. Parkin, M. Hayashi, and L. Thomas, Science **320**, 190 (2008).
[12] L. R. Walker, Bell Telephone Laboratories Memorandum, 1956 (unpublished); see, however, the presentation by Dillon [40] and the later paper by Schryer and Walker [14].
[13] J. C. Slonczewski, Int. J. Magn. **2**, 85 (1972).
[14] N. L. Schryer and L. R. Walker, J. Appl. Phys. **45**, 5406 (1974).
[15] A. P. Malozemoff and J. C. Slonczewski, *Magnetic Domain Walls in Bubble Materials* (Academic, New York, 1979).
[16] A. H. Bobeck, I. Danylchuk, J. P. Remeika, L. G. van Uitert, and E. M. Walters, in *Proceedings of the International Conference on Ferrites 1970* (University of Tokyo Press, Tokyo, 1971), p. 361.
[17] B. E. Argyle, J. C. Slonczewski, and A. F. Mayadas, in *Magnetism and Magnetic Materials 1971 Parts 1 and 2*, AIP Conf. Proc. No. 5 (AIP, New York, 1972), p. 175.
[18] F. H. de Leeuw, IEEE Trans. Magn. **14**, 596 (1978).
[19] V. V. Volkov, V. A. Bokov, and V. I. Karpovich, Sov. Phys. Solid State **24**, 1315 (1982).
[20] J. C. Slonczewski, in *Magnetism and Magnetic Materials 1971 Parts 1 and 2*, AIP Conf. Proc. No. 5 (AIP, New York, 1972), p. 170.
[21] A. Dourlat, V. Jeudy, A. Lemaître, and C. Gourdon, Phys. Rev. B **78**, 161303(R) (2008).
[22] C. Gourdon, L. Thevenard, S. Haghgoo, and A. Cebers, Phys. Rev. B **88**, 014428 (2013).
[23] Y. Yoshimura, K.-J. Kim, T. Taniguchi, T. Tono, K. Ueda, R. Hiramatsu, T. Moriyama, N. Yamada, Y. Nakatani, and T. Ono, Nat. Phys. **12**, 157 (2016).
[24] T. H. Pham, J. Vogel, J. Sampaio, M. Vaňatka, J.-C. Rojas-Sanchez, M. Bonfim, D. S. Chaves, F. Choueikani, P. Ohresser, E. Otero, A. Thiaville, and S. Pizzini, Europhys. Lett. **113**, 67001 (2016).
[25] F. Ajejas, V. Krizakova, D. de Souza Chaves, J. Vogel, P. Perna, R. Guerrero, A. Gudin, J. Camaraero, and S. Pizzini, Appl. Phys. Lett. **111**, 202402 (2017).
[26] K. Yamada and Y. Nakatani, Appl. Phys. Express **8**, 093004 (2015).
[27] D. de Souza Chaves, Ph.D. thesis, Université Grenoble Alpes, 2018.
[28] A. Vansteenkiste, J. Leliaert, M. Dvornik, M. Helsen, F. Garcia-Sanchez, and B. Van Waeyenberge, AIP Adv. **4**, 107133 (2014).
[29] O. Boulle, S. Rohart, L. D. Buda-Prejbeanu, É. Jué, I. M. Miron, S. Pizzini, J. Vogel, G. Gaudin, and A. Thiaville, Phys. Rev. Lett. **111**, 217203 (2013).
[30] To define a winding sense, the DW needs to be oriented. For the magnetic bubbles, there is a natural way to do it [15] as the bubble has an interior.
[31] R. Cheng, M. Li, A. Sapkota, A. Rai, A. Pokhrel, T. Mewes, C. Mewes, D. Xiao, M. De Graef, and V. Sokalski, Phys. Rev. B **99**, 184412 (2019).
[32] A. Hubert and R. Schäfer, *Magnetic Domains* (Springer, Berlin, 1998).
[33] A. Hubert, in Magnetism and Magnetic Materials 1973: Nineteenth Annual Conference, *AIP Conf. Proc.* No. 18 (AIP, New York, 1974), p. 178.
[34] Y. Nakatani and N. Hayashi, IEEE Trans. Magn. **23**, 2179 (1987).
[35] J. C. Slonczewski, J. Appl. Phys. **44**, 1759 (1973).
[36] J. C. Slonczewski, J. Appl. Phys. **45**, 2705 (1974).
[37] S. Lemerle, J. Ferré, C. Chappert, V. Mathet, T. Giamarchi, and P. Le Doussal, Phys. Rev. Lett. **80**, 849 (1998).
[38] A. Thiaville, Y. Nakatani, F. Piéchon, J. Miltat, and T. Ono, Eur. Phys. J. B **60**, 15 (2007).
[39] A. Thiaville and J. Miltat, in *Topology in Magnetism*, edited by J. Zang, V. Cros, and A. Hoffmann, Springer Series in Solid-State Sciences Vol. 192 (Springer, Cham, 2018), pp. 41–73.
[40] J. F. Dillon, Jr., in *Magnetism*, edited by G. Rado and H. Suhl (Academic, New York, 1963), Vol. 3, pp. 415–464.